RSC Advances

PAPER

View Article Online
View Journal | View Issue

Cite this: *RSC Adv.*, 2021, **11**, 34945

meta-Terphenyl linked donor–π–acceptor dyads: intramolecular charge transfer controlled by electron acceptor group tuning†

Min-Ji Kim, Mina Ahn, Minjung Chae, Sanghyun Kim, Daehoon Kim and Kyung-Ryang Wee *

Received 2nd September 2021
Accepted 21st October 2021

DOI: 10.1039/d1ra06602a

rsc.li/rsc-advances

A series of *meta*-terphenyl linked donor–π–acceptor (D–π–A) dyads were prepared to understand the electronic effects of a *meta*-terphenyl linker according to the electron-accepting ability change. The energy band gaps of the dyads were controlled by tuning the accepting ability, which resulted in emission colors ranging from blue-green to red. In the Lippert–Mataga plots, intramolecular charge transfer (ICT) behavior was observed, which showed gradually increased ICT characteristics as the accepting ability was increased. On the other hand, in the absorption spectra, a red shift of the ICT transition was observed differently from the electron-accepting ability tendency. Thus, the experimental results show that the ICT is determined by steric hindrance rather than the acceptor ability in the ground state due to the lack of π-conjugation of the terphenyl linker by the electron node in the *meta*-position, whereas ICT in the excited state is controlled by electron-accepting ability.

Introduction

Diverse dipolar organic materials, consisting of electron-donor (D) and electron-acceptor (A) units with various π-linkers, have been investigated and applied to various research areas because of their unique electrochemical and photophysical properties.[1–9] In particular, donor–π–acceptor (D–π–A) dyad molecules are widely used molecular systems because of the easy tailoring of the photophysical property by changing the sub-units such as donor, acceptor, and π-linker. Thus, an adequate combination of sub-units in the D–π–A dyad system is the key to achieving the desired electrochemical and photophysical properties for a wide range of applications, such as organic light-emitting diodes (OLEDs),[10–17] dye-sensitized solar cells (DSSCs),[18–21] organic photovoltaics (OPVs),[22–24] photoelectrochemical cells (PECs),[25–28] fluorescence sensors,[29–31] mechanochromic materials,[32–34] nonlinear optical materials,[35,36] and nanostructured materials.[37–39]

The notable features of D–π–A dyads are intramolecular charge transfer (ICT) and photoinduced electron transfer (PET) in the ground and excited states because of the large electronic dipoles. The PET and ICT properties in D–π–A dyads are entirely different phenomena. In the excited state, ICT is partial charge transfer process from the donor to the acceptor whereas PET is a unit electron transfer process.[40,41] They are used in other research areas according to the difference in the ICT and PET characteristics. Generally, the characteristic ICT absorption and emission are vital in determining the optical and electronic properties.[42–44] In addition, the ICT absorption and emission properties can be finely controlled by changing the donor, acceptor, π-linker units, and molecular geometry, which can result in an effective bandgap and color tuning. PET process can be called charge separation by unit electron transfer, and reverse electron transfer are called charge recombination processes.[40] PET systems with high-efficiency charge separation and slow charge recombination processes play an essential role in improving the photovoltaic performance.[45]

Recently, *ortho*-, *meta*-, and *para*-terphenyl π-linker-based D–π–A dyads, comprised of triphenylamine (TPA) as a donor and 1-phenyl-1*H*-benzimidazole (IMI) as an acceptor, were examined to understand the effects of geometric isomerism of D–π–A dyads.[46] To clarify the distinction between ICT and PET occurring in the three terphenyl isomeric D–π–A dyads, the three terphenyl backbone-based isomers were compared, and all isomers showed distinctive ICT emission rather than PET in the excited state. In particular, the non-conjugated system of the *meta*-terphenyl isomer D–π–A dyads also showed ICT emission and were distinguished with previously reported non-conjugated D–π–A dyads because of its unique *meta*-terphenyl conjugation system. *meta*-Terphenyl is a non-conjugated molecular system caused by the electronically nodal site at

Department of Chemistry, Institute of Natural Science, Daegu University, Gyeongsan 38453, Republic of Korea. E-mail: krwee@daegu.ac.kr

† Electronic supplementary information (ESI) available: NMR spectra; GC-MS data; X-ray crystallographic data of **Tria**; absorption and emission spectra of TPA donor; absorption and emission spectra in various solvents and solid state; emission lifetime profile; Lippert–Mataga plots and dipole moment values; CV; HOMO and LUMO energy; DFT/TD-DFT calculation results. CCDC 2091706 (**Tria**). For ESI and crystallographic data in CIF or other electronic format see DOI: 10.1039/d1ra06602a

meta-position, and only two phenyl units are conjugated. Because of these electronic properties, various *meta*-position-linked molecules, including *meta*-terphenyl-containing materials, have been developed and used widely, especially in the development of wide bandgap materials.[47–50] These compounds are also one of the frequently used conjugation braking methods in the development of bifunctional materials.[51,52] On the other hand, the *meta*-position-linked molecular system is also discriminated from the conventional conjugation braking systems and not completely separated electronically between the two functional units. Although the study on the influence of a *meta*-linkage on the electronic coupling had been reported, information on the electronic nodal-position effect on the *meta*-terphenyl as a linker is still limited.[53–56]

In this regard, a series of *meta*-terphenyl linked D–π–A dyads were designed and prepared to understand the electronic effects of the *meta*-terphenyl linker in the D–π–A dyads. In the *meta*-terphenyl linked D–π–A dyads, the electron-donating group was used a TPA unit because it is one of the well-known efficient donor units.[57,58] In addition, four different electron-withdrawing groups (cyanide, benzoxazole, benzothiazole, and 2,4-diphenyl-1,3,5-triazine) were selected for their varying electron affinity capability with steric effects. The electronic and steric effects on the electron-withdrawing groups were considered to clarify the *meta*-terphenyl electronic nodal-position effect. Basically, the 2,4-diphenyl-1,3,5-triazine moiety has strong electron-accepting ability among the four different electron-withdrawing groups and a bulky structure.[59] Benzoxazole and benzothiazole moieties have relatively weaker electron-accepting ability and planar molecular structures compared to 2,4-diphenyl-1,3,5-triazine, and they were selected to compare only the electronic effect.[60,61] For the cyanide moiety, the electron-acceptor ability is weakest among the electron-withdrawing groups, and it has the least steric hindrance.[59] The *meta*-terphenyl electronic nodal-position effects with ICT control were investigated depending on the electron-withdrawing groups. The photophysical and electrochemical properties including ICT properties, were examined and density functional theory (DFT) calculations were performed. In particular, distinctive ICT emissions depending on the electron-withdrawing group were compared to understand the electronic nodal-position effects on the *meta*-terphenyl by changing the electron-withdrawing group.

Results and discussion

Synthesis and structure characterization

Scheme 1 shows the synthetic procedure for *meta*-terphenyl linked D–π–A dyads. The starting materials, (4-(diphenylamino) phenyl)boronic acid, 4-(4,4,5,5-tetramethyl-1,3,2-dioxaborolan-2-yl)benzonitrile, 2-(4-(4,4,5,5-tetramethyl-1,3,2-dioxaborolan-2-yl)phenyl)benzo[*d*]oxazole, (4-(benzo[*d*]thiazol-2-yl)phenyl) boronic acid, and 2,4-diphenyl-6-(4-(4,4,5,5-tetramethyl-1,3,2-dioxaborolan-2-yl)phenyl)-1,3,5-triazine, were prepared according to the previously reported procedures.[62] All dyads were then synthesized using two-step palladium-catalyzed Suzuki–Miyaura coupling reactions with triphenylamine (TPA) as an electron donor, and cyanide, benzoxazole, benzothiazole, and 2,4-diphenyl-1,3,5-triazine as an electron acceptor. All four compounds were purified by silica gel column chromatography and showed yields in the range of 15 to 75% due to solubility issues. The molecular structures of all products were determined by ^{1}H- and ^{13}C{^{1}H}-nuclear magnetic resonance (NMR) spectroscopy (Fig. S1–S8†),[63,64] elemental analysis, and mass spectrometry (Fig. S9†). Finally, the structures of **Tria** were authenticated by single-crystal X-ray crystallography. The Experimental section and ESI† provide details of the synthetic procedures and characterization data.

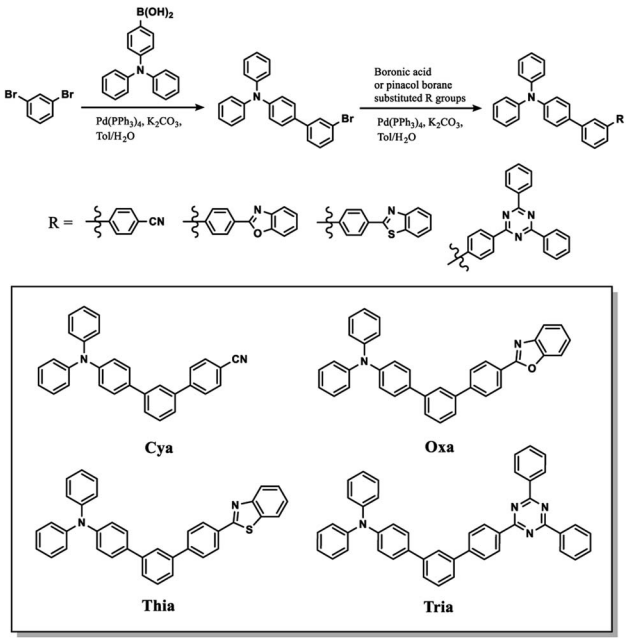

Scheme 1 Synthetic routes of **Cya**, **Oxa**, **Thia**, and **Tria**.

For X-ray crystallographic analysis, a single crystal of **Tria** was grown by slow evaporation in a CH_2Cl_2/*n*-hexane mixture at room temperature. The **Tria** crystal was triclinic in the $P\bar{1}$ space group. Table S1† lists the detailed crystallographic data for the molecule, and Fig. S10† shows Oak Ridge thermal ellipsoid plot (ORTEP) drawings of **Tria**. In the packing diagram (Fig. 1b and c), the **Tria** molecules were stacked in a β packing (sheet-like packing) type.[65] The degree of π-conjugation of **Tria** in the solid-state was determined by the terphenyl torsion angles. In the X-ray structure (Fig. 1a), the angle between the central benzene and the phenyl

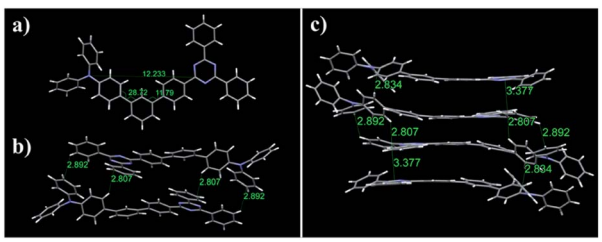

Fig. 1 (a) Crystal structure diagram of **Tria**. (b) Molecular packing of the dimeric structures of **Tria**. (c) Crystal packing diagram of **Tria**.

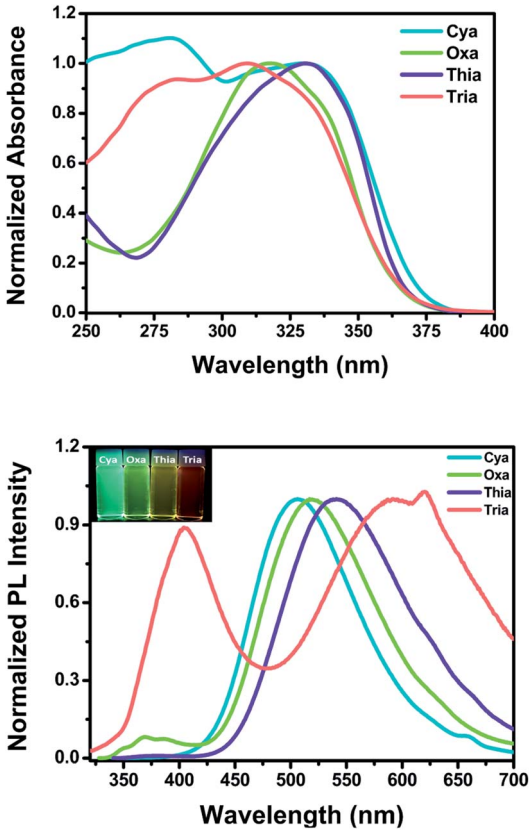

Fig. 2 UV-vis absorption (top) and emission (bottom) spectra of **Cya**–**Tria** in CH_2Cl_2. Insets: photographs of **Cya**–**Tria** in CH_2Cl_2 solution under UV irradiation at 365 nm.

bound to the TPA moiety was *ca.* 28.72° (C20–C19–C16–C15), and that between the central benzene and the phenyl bound to the triazine moiety was *ca.* 11.79° (C20–C21–C25–C26), suggesting that the triazine moiety is more planar than TPA in the solid state. The intramolecular distance between the N atom of TPA and the C atom of triazine bound to terphenyl was 12.2 Å (Fig. 1a), which agreed with the DFT calculated value (12.4 Å). Based on the results obtained for **Tria**, we assumed that the molecular structures of the dyads were reliably predicted by DFT calculation. As shown in Fig. S16,† the dihedral angle for **Cya**, **Oxa**, **Thia**, and **Tria** between the phenyl rings close to acceptor moiety were 37.2°, 36.8°, 36.6°, and 37.0°, respectively. The distance from the central benzene to the acceptor moiety increased in the order of **Cya** (9.7 Å) < **Oxa** (13.0 Å) < **Thia** (13.3 Å) < **Tria** (13.9 Å). Therefore, as a result of considering the two factors of dihedral angle and distance, it indicates bulkiness of dyads increased in the order of **Cya** < **Oxa** < **Thia** < **Tria**.

Photophysical properties

Fig. 2 shows the steady-state UV-visible absorption and emission spectra of **Cya**–**Tria**, and Table 1 lists the spectral parameters. In the UV-visible absorption spectra (Fig. S11†), all dyads showed an absorption band at 275–346 nm, which was attributed to a locally excited (LE) transition of the donor and each acceptor moieties. The shoulder hidden in the broad absorption band at ~350 nm corresponds to the ^{1}ICT ← S_0 transition, which means an intramolecular interaction in the ground state. For **Thia**, the ICT transition was more red-shifted than **Oxa** in the absorption spectrum due to the strong acceptor ability. The red shift of the ICT transition was expected in the order of strong acceptor ability, **Cya** < **Oxa** < **Thia** < **Tria**, but the ICT transition was red-shifted in the order of **Tria**, **Oxa** < **Thia** < **Cya**. According to a previous report, compared to the well-conjugated *para*-terphenyl, the *meta*-terphenyl linker has weak electron coupling between donor and acceptor because only two phenyl units are conjugated by the electron node.[40] From this point of view, this tendency suggests that ICT is determined by steric hindrance rather than the acceptor ability at the ground state, because of the lack of π-conjugation of the terphenyl linker by the electron nodes in the *meta*-position. The acceptor moiety of **Tria** has relatively stronger acceptor ability than the other compounds, but weak electron coupling between the donor and acceptor occurs because of its nonplanar molecular structure. In contrast, the acceptor ability of **Cya** is relatively weak, but the steric hindrance is small, resulting in strong coupling between the donor and acceptor. In the case of **Oxa** and **Thia**, the acceptor moieties have a more planar molecular structure than **Tria** and less steric hindrance. Hence, the ICT transition is observed with a red shift than that of **Tria** in the absorption spectrum. The thin-film absorption and emission spectra were also measured to examine the intermolecular interactions (Fig. S12†). The thin-film absorption and emission spectra of **Cya**–**Tria** exhibited red shifts compared to the corresponding

Table 1 Photophysical properties of **Cya**, **Oxa**, **Thia**, and **Tria**

	λ_{abs} (nm)		λ_{em} (nm)		Stokes shift (cm^{-1})	Φ_{em} [c]	τ_{em} [d] (ns)	k_{rad} [e] × 10^7 (s^{-1})	k_{nr} [e] × 10^7 (s^{-1})	k_{rad}/k_{nr}
	Sol (ε)[a]	Film[b]	Sol[a]	Film[b]						
Cya	281, 329 (65 308)	351	506	441	10 632	0.099	3.05, 22.43	3.24, 0.44	29.5, 4.02	0.11, 0.11
Oxa	318, 338 (76 225)	333	368, 517	442	10 243	0.020	2.68, 22.22	0.75, 0.09	36.57, 4.41	0.02, 0.02
Thia	331, 346 (72 182)	357	375, 541	388, 459	10 417	0.012	21.86	0.055	4.52	0.012
Tria	309, 330 (66 976)	334	405, 591	390, 486	13 382	0.0096	5.18, 38.94	0.19, 0.025	19.12, 2.54	0.01, 0.01

[a] Measured in 1×10^{-5} M CH_2Cl_2 at room temperature (RT). [b] Measured from a drop-casted film on glass. [c] Fluorescence quantum yields, with 9,10-diphenylanthracene ($\Phi_{PL} = 0.95$, ethanol) as the standard, in CH_2Cl_2 at RT. [d] Fluorescence lifetime measured in CH_2Cl_2. [e] Values of k_{rad} and k_{nr} were calculated using $k_{rad} = \Phi_{em}/\tau_{em}$ and $k_{nr} = (1/\tau_{em}) - k_{rad}$, respectively.

spectra in an *n*-hexane solution, suggesting that all dyads formed J-aggregates.[66]

Except for **Cya**, all dyads exhibited dual emission at approximately 375 nm and at a longer wavelength region of 506–591 nm in a CH_2Cl_2 solution (Fig. 2 (bottom)). The emission at short wavelengths can be assigned to the fluorescence from the locally excited state. In the case of **Cya**, no emission spectrum was observed at short wavelengths because electron coupling between the donor and acceptor is favored by the small steric hindrance of the cyano group. The long-wavelength emission was red-shifted in the order **Cya** < **Oxa** < **Thia** < **Tria**. The emission profiles ranged from blue-green to red, indicating that the emission color was tuned by the accepting ability. The emission at long-wavelengths was assigned to the fluorescence from the ICT state. These results suggest that the ICT is tuned by the electron-accepting ability in the excited state. In other words, the *meta*-position effect by the electron nodes has more influence in the ground state than in the excited state. For **Tria**, a greater Stokes shift of ICT transition in CH_2Cl_2 was observed than the other dyads, indicating relatively larger structural reorganization energy due to photo-excitation from the ground state to the excited state.

To further understand the properties of the excited state for the dyads, fluorescence quantum yield (Φ_{em}) and fluorescence lifetime (τ_{em}) measurements were performed in CH_2Cl_2; the results are shown in Table 1. Similar to the *meta*-position-based dyad reported previously, the quantum yields for the dyads were in the range of 0.099–0.0096 because of the deactivation pathways from the excited state caused by the electron nodes of terphenyl *meta*-positions.[46] The fluorescence lifetime measurements performed on **Cya**, **Oxa**, and **Tria** exhibited biexponential fluorescence decays. In contrast, **Thia** exhibited single exponential fluorescence decay (Fig. S13†). As reported previously, for **Cya** and **Oxa**, the slow process of the biexponential fluorescence decay was attributed to charge transfer from the donor to acceptor moieties and the fast process of the biexponential fluorescence decay was attributed to charge transfer centered in and around TPA.[46] In the case of **Thia**, the strong charge transfer from the donor to acceptor rather than the charge transfer centered in and around TPA by the strong acceptor of the planar structure would be favored. Therefore, single exponential fluorescence decay is attributed to the strong charge transfer. Because **Tria** has a strong acceptor with a nonplanar structure, it was assumed that the slow process of the biexponential fluorescence decay could be attributed to charge transfer from TPA to two phenyls of triazine. The rapid process of the biexponential fluorescence decay can be attributed to charge transfer from TPA to the triazine center. As the electron-accepting ability of the substituent increases, the fluorescence quantum yield decreases, and the lifetime increases. These results can be explained mainly by the radiative and nonradiative decay rate constants (k_{rad} and k_{nr}), which were calculated from the Φ_{em} and τ_{em} values (Table 1). All dyads have relatively larger k_{nr} values than k_{rad}, indicating that the nonconjugated structure of the dyads favors nonradiative decay. In addition, as the electron-accepting ability of the substituent increases, the k_{rad} value tended to decrease overall, but the k_{nr} value did not. This means that the electron-accepting ability of the substituent controls the k_{rad} value. Hence, the k_{rad} value plays a key role in controlling the emission color.

Solvatochromic properties

The absorption and emission behaviors of the *meta*-position-based dyads were investigated in various solvents to study the solvatochromic effect (Table S2 and Fig. S14†). The absorption spectra of all dyads showed a weak solvent polarity dependency. In contrast, the emission spectra of **Cya**–**Tria** showed a marked red shift with increasing solvent polarity from *n*-hexane to acetonitrile, indicating the presence of the ICT state in the excited state (Fig. 3). In addition, the solvatochromic shift in the emission spectra increased gradually from **Cya** to **Tria**, meaning that it has strong ICT properties as the electron-accepting ability of the substituent increases.

The dipole moments between the ground and excited states using a Lippert–Mataga plot were analyzed to understand the solvation effects better. The Stokes shift was plotted as a function of the solvent polarity parameter using eqn (1):[67]

$$\Delta\nu = \overline{\nu_a} - \overline{\nu_f} = \frac{2}{hca_0{}^3}\left(\frac{\varepsilon-1}{2\varepsilon+1} + \frac{n^2-1}{2n^2+1}\right) \times \left(\mu_e - \mu_g\right)^2 + \text{constant}$$
$$= 2\Delta f \times \frac{\Delta\mu^2}{hca_0{}^3} + \text{constant} \quad (1)$$

where $\Delta\nu$ is the Stokes shift; $\mu_e - \mu_g$ ($\Delta\mu$) is the difference between the dipole moments of excited and ground states; c, h, and a_0 is the speed of light; Planck's constant, and the radius of the Onsager cavity around the fluorophore, respectively. The solvent dielectric constant (ε) and refractive index (n) are included in the term Δf, which is known as the solvent polarity parameter. The Onsager radii were determined by *ab initio* calculations and were considered to be half of the average molecular sizes of **Cya**, **Oxa**, **Thia**, and **Tria** (18.3, 22.6, 22.8, and 23.9 Å, respectively). Table S3† lists the values of ground-state dipole moments (μ_g) for the energy-minimized structures obtained using the DFT method. The excited-state dipole

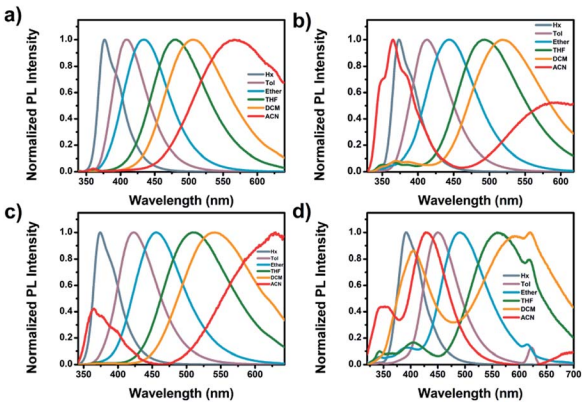

Fig. 3 Emission spectra of (a) **Cya**, (b) **Oxa**, (c) **Thia**, and (d) **Tria** measured in various solvents.

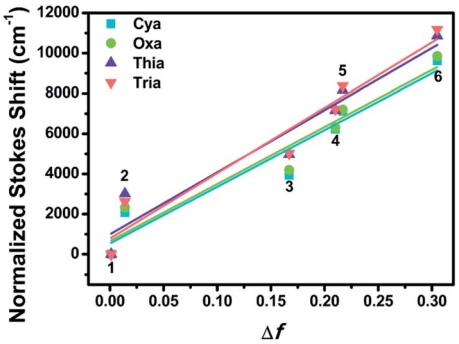

Fig. 4 Lippert–Mataga plots of **Cya**–**Tria** in various solvents: 1, *n*-hexane; 2, toluene; 3, ethyl ether; 4, THF; 5, CH_2Cl_2; 6, CH_3CN.

moments (μ_e) were calculated using the ground state dipole moment (μ_g) and dipole moment change ($\Delta\mu$).

The ground state dipole moments for **Cya**, **Oxa**, **Thia**, and **Tria** were 5.92, 1.98, 1.52, and 0.94 D, respectively, which increases with increasing degree of asymmetry of the dyads. On the other hand, the excited state dipole moment increased in the order of **Cya** (40.41 D) < **Oxa** (61.69 D) < **Thia** (65.73 D) < **Tria** (73.39 D) as the electron-accepting ability increased. Hence, the excited state dipole moments for **Cya**–**Tria** are significantly greater than the ground state dipole moment, qualitatively showing a small charge transfer gap in the ground state and a large charge transfer gap in the excited state, as measured by steady-state UV-vis absorption and emission spectroscopy. Unlike the excited state dipole moment, the tendency of the ground state dipole moment did not coincide with the accepting ability, which suggests that ICT control by the accepting ability is controlled only in the excited state. Fig. 4 and S15† presents the plots of $\Delta\nu$ *versus* Δf for four dyads, showing the linear correlation between these two factors. The trend in the slope of the Lippert–Mataga plots follows the order **Cya** < **Oxa** < **Thia** < **Tria**, and the slope of the Lippert–Mataga plot quantitatively represents the ICT process in the excited state. Hence, **Tria** has strong ICT character than other dyads. These results indicate that the ICT properties of *meta*-position-based dyads are controlled by their electron-accepting ability.

Electrochemical properties

Cyclic voltammetry (CV) was performed to evaluate the electrochemical properties of *meta*-terphenyl linked donor–π–acceptor dyads in CH_2Cl_2 and THF, using a three-electrode cell system, with glassy carbon, platinum wire, and SCE as the working, counter, and reference electrodes, respectively (Fig. 5). All dyads showed reversible oxidation peaks with oxidation onsets at 0.92, 0.90, 0.92, and 0.91 V for **Cya**, **Oxa**, **Thia**, and **Tria**, respectively, because the dyads had the same electron donor moiety. Hence, the dyads have a similar highest occupied molecular orbital (HOMO) energy level. In contrast, for a reversible reduction peak, the onset potentials of the first reduction were shifted anodically in the order of **Cya** (−1.89 V) < **Oxa** (−1.79 V) < **Thia** (−1.00 V) < **Tria** (−0.98 V). This tendency reflects the greater enhancement of the electron-accepting ability when going from **Cya** to **Tria**. Furthermore, for **Tria**, the first and second reduction peaks were close, suggesting that the lowest unoccupied molecular orbital (LUMO) and LUMO + 1 energy levels would be close.

The experimental and calculated HOMO–LUMO energy levels of the *meta*-terphenyl linked donor–π–acceptor dyads were compared (Table 2). The experimental HOMO energy levels could be determined from the oxidation onset potentials, and the HOMO energy levels of **Cya**–**Tria** were estimated to be *ca.* −5.72 to −5.71 eV. The experimental LUMO energy levels were estimated to be *ca.* −2.91 to −3.82 eV from the reduction onset potentials. The experimental LUMO levels decreased with increasing electron-accepting ability with a maximum difference of 0.91 eV. In contrast, the experimental HOMO levels were changed slightly, indicating that the LUMO levels were susceptible to the electronic variations of the substituents. The calculated HOMO energy levels ranged from −5.08 to −4.97 eV, and the calculated LUMO energy levels ranged from −1.65 to −1.88 eV. The calculated values were higher than the experimental values for all compounds, but the tendencies were similar. These results show that an increase in the electron-accepting ability stabilizes the LUMO more than the HOMO, narrowing the bandgap and controlling the emission color.

Density functional theory (DFT)

Fig. 6 and S17–S20† presents the HOMO and LUMO orbitals of *meta*-terphenyl linked donor–π–acceptor dyads, which were obtained using Gaussian 16 and visualized using Chem3D and GaussView programs. The geometries were optimized by the DFT method using the B3LYP correlation function employing the 6-31G(d,p) level in the vacuum state.[68–70] In all dyads studied, the HOMO was distributed mainly on the TPA moiety, and the LUMO was strongly localized on each acceptor moiety. These changes in the orbital distributions of the HOMOs and

Table 2 Energy band gap properties of **Cya**, **Oxa**, **Thia**, and **Tria**

	HOMO[a] (eV)	LUMO[b] (eV)	E_g (eV)	HOMO[c] (eV)	LUMO[c] (eV)	E_g^{cal} (eV)
Cya	−5.72	−2.91	2.81	−5.08	−1.65	3.43
Oxa	−5.70	−3.01	2.69	−4.99	−1.60	3.39
Thia	−5.72	−3.80	1.92	−4.99	−1.71	3.28
Tria	−5.71	−3.82	1.89	−4.97	−1.88	3.09

[a] E_{HOMO} (eV) $= -e(E_{onset}^{ox} + 4.8)$. [b] E_{LUMO} (eV) $= -e(E_{onset}^{red} + 4.8)$. [c] Obtained by DFT calculation.

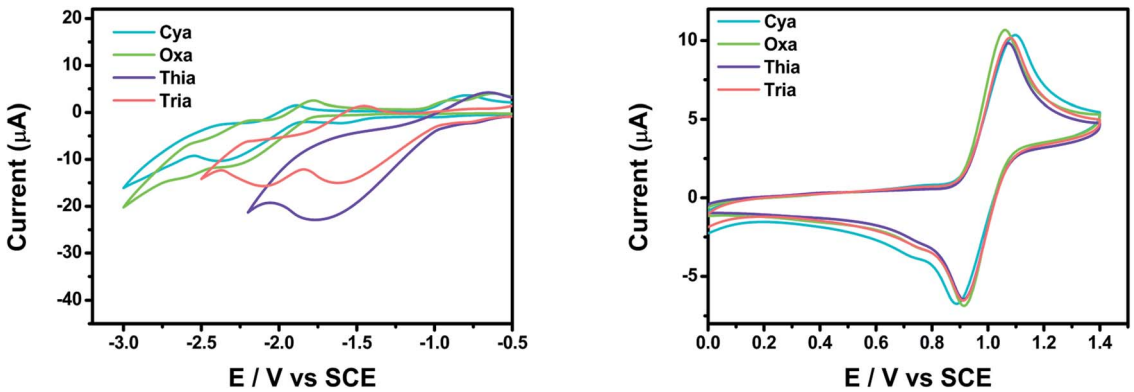

Fig. 5 CV curves of **Cya**, **Oxa**, **Thia**, and **Tria**. The reduction potentials (left) were measured in THF and the oxidation potentials (right) in CH_2Cl_2. In all experiments, the electrolyte was 0.1 M TBAP and was measured at a scan rate of 0.05 V s^{-1}.

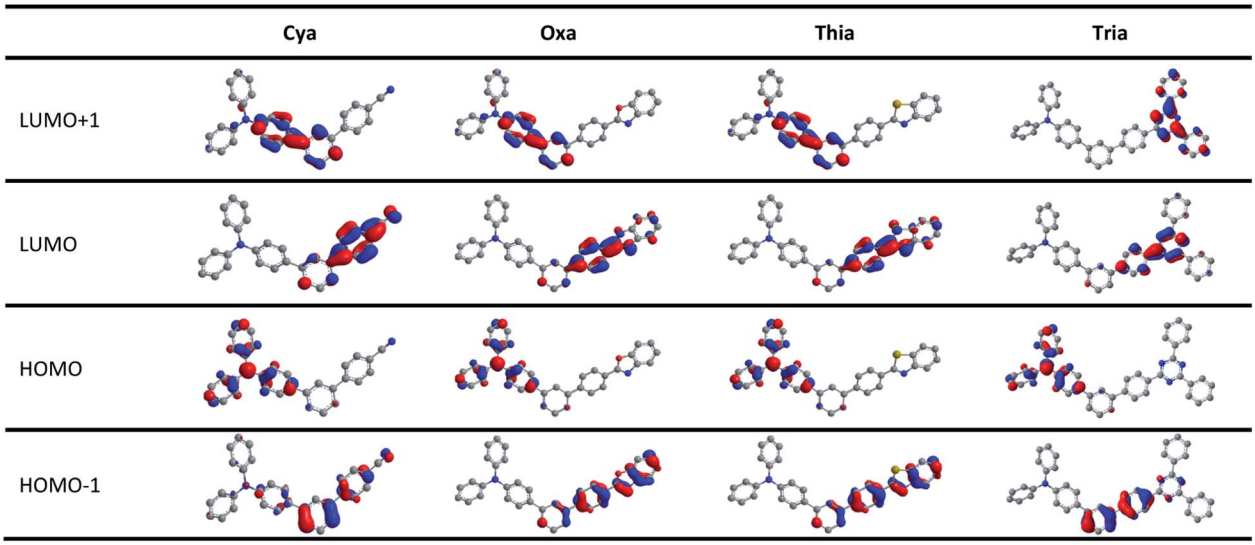

Fig. 6 Frontier orbital distributions (HOMO − 1, HOMO, LUMO, LUMO + 1) of **Cya**, **Oxa**, **Thia**, and **Tria** calculated by DFT with the B3LYP function and the 6-31G(d,p) basis.

LUMOs showed that charge transfer occurs from the donor to acceptor in the excited state. The *meta*-terphenyl structure is conjugated at only two phenyl units because of the electronic nodes at the *meta*-position. In addition, the LUMOs of dyads were extended to the acceptor moiety rather than *meta*-terphenyl linker in the order **Cya** < **Oxa** < **Thia** < **Tria**, indicating that it is controlled by the accepting ability. Unlike the other dyads, the LUMO + 1 of **Tria** was centered mainly on the two phenyl groups of triazine moiety. These orbital distributions suggest that the fluorescence decay profile and electrochemical properties of **Tria** were determined by the nonplanar structure and strong electron-accepting ability of triazine.

As shown in Fig. S21–S24 and Tables S9–S12 of ESI,† time-dependent density functional theory (TD-DFT) calculations were carried out at the same functional and basis set. For all dyads, the lowest-energy singlet transition involved the LUMO ← HOMO transitions; all were ICT transitions from the donor to acceptor. These transitions of **Cya**, **Oxa**, **Thia**, and **Tria** are very weak, with oscillator strengths between 0.0156–0.0035. On the other hand, the LUMO + 1 ← HOMO transitions of **Cya**, **Oxa**, and **Thia**, and the LUMO + 2 ← HOMO transitions of **Tria** are very strong with oscillator strengths between 0.6835–1.257, showing that all are transitions centered in and around TPA. These results are because the substitution of the terphenyl linker at the *meta*-position causes the nodal site in the HOMO and LUMO. Furthermore, the LUMO ← HOMO transition shifts theoretically followed the order, **Cya** (400 nm), **Oxa** (402 nm), **Thia** (416 nm), and **Tria** (439 nm), which are consistent with the electron-accepting ability. Nevertheless, the experimental results were different from the theoretical results, suggesting that the properties of *meta*-terphenyl linked donor–π–acceptor dyads in the ground state should consider steric hindrance rather than the electron-accepting ability.

Conclusions

meta-Terphenyl linked donor–π–acceptor (D–π–A) dyads were designed and synthesized to understand the electronic effects

of the *meta*-terphenyl linker in the D–π–A dyads. By modulating their electron-accepting ability by introducing cyanide, benzoxazole, benzothiazole, and 2,4-diphenyl-1,3,5-triazine moieties, the photophysical and electrochemical properties of the four dyads were investigated and compared. In the steady-state emission spectra, the long-wavelength emission was red-shifted in the order of strong acceptor ability, **Cya** < **Oxa** < **Thia** < **Tria**, and a bathochromic shift property was observed with increasing solvent polarity. These results showed that the ICT was tuned by the electron-accepting ability in the excited state. Similarly, the Lippert–Mataga plot and cyclic voltammetry curves were consistent with the electron-accepting ability. On the other hand, in the steady-state absorption spectra, the ICT transition was red-shifted in the order of **Tria**, **Oxa** < **Thia** < **Cya**, and was different from the electron-accepting ability tendency. Hence, ICT is determined by steric hindrance rather than the acceptor ability at the ground state due to the *meta*-position effect by the electron nodes. These results highlight the need to consider ICT modulation in the ground and excited states of *meta*-terphenyl linked donor–π–acceptor dyads with an electron node.

Experimental

General information

Based on standard Schlenk techniques, all of the synthesis experimental procedures were performed under a dry argon condition. Reagents and solvents were purchased from commercial sources and used as received without further purification, unless otherwise stated. All reactions were monitored with thin layer chromatography (TLC) using commercial TLC plates (Merck Co.). Silica gel column chromatography was performed on silica gel 60 G (230–400 mesh ASTM, Merck Co.). The synthesized compounds were characterized by ^{1}H-NMR or ^{13}C{^{1}H}-NMR, and elemental analysis. The ^{1}H and proton-decoupled ^{13}C spectra were recorded on a Bruker 500 spectrometer operating at 500 and 125 MHz, respectively, and all proton and carbon chemical shifts were measured relative to internal residual chloroform (99.5% $CDCl_3$) from the lock solvent. The elemental analyses (C, H, N, O, S) were performed using Thermo Fisher Scientific Flash 2000 series analyzer. The GC-MS analysis was performed using a highly sensitive Gas Chromatograph/Mass Selective Detector spectrometer (Agilent, 7890B-5977B GC/MSD). The crystal structure was determined by single-crystal X-ray diffractometer at the Western Seoul Center of Korea Basic Science Institute.

Synthesis of 4″-(diphenylamino)-[1,1′:3′,1″-terphenyl]-4-carbonitrile (Cya)

A mixture of 3′-bromo-*N*,*N*-diphenyl-[1,1′-biphenyl]-4-amine (0.38 g, 0.95 mmol), 4-(4,4,5,5-tetramethyl-1,3,2-dioxaborolan-2-yl)benzonitrile (0.3 g, 1.33 mmol), $Pd(PPh_3)_4$ (10 mol%), K_2CO_3 (0.66 g, 4.75 mmol) in toluene/H_2O (v/v = 40 mL/10 mL) was refluxed under argon at 110 °C for overnight. After cooling to room temperature, deionized water (50 mL) was poured and organic layer was separated using a separating funnel. The water layer was washed using methylene chloride (×3) for extracted remained organic residue. After combined all of organic solvents, the organic layer was dried over anhydrous $MgSO_4$ and then filtered off. The solvent was removed under reduced pressure, and the residue was purified by silica gel column chromatography using dichloromethane/*n*-hexane (v/v = 1 : 2) as the eluent and obtained light yellow powder. Yield: 0.22 g, 55%. ^{1}H NMR (500 MHz, $CDCl_3$, ppm) δ 7.76 (s, 1H), 7.74 (s, 4H), 7.63–7.61 (m, 1H), 7.53–7.52 (m, 2H), 7.50 (d, J = 9.0 Hz, 2H), 7.27 (t, J = 7.5 Hz, 4H), 7.15 (t, J = 7.0 Hz, 6H), 7.05 (t, J = 7.5 Hz, 2H). ^{13}C{^{1}H} (125 MHz, $CDCl_3$, ppm) δ 147.66, 147.60, 145.76, 141.74, 139.73, 134.35, 132.63, 129.53, 129.34, 127.85, 126.98, 125.68, 125.63, 124.58, 123.74, 123.15, 118.92, 111.06. GC-MS (*m*/*z*) calcd for $C_{31}H_{22}N_2$: 422.53, found: 422.3 $[M]^+$. Anal. calcd for $C_{31}H_{22}N_2$: C, 88.12; H, 5.25; N, 6.63. Found: C, 88.17; H, 5.24; N, 6.59.

Synthesis of 4″-(benzo[*d*]oxazol-2-yl)-*N*,*N*-diphenyl-[1,1′:3′,1″-terphenyl]-4-amine (Oxa)

A mixture of 3′-bromo-*N*,*N*-diphenyl-[1,1′-biphenyl]-4-amine (0.45 g, 1.13 mmol), the 2-(4-(4,4,5,5-tetramethyl-1,3,2-dioxaborolan-2-yl)phenyl)benzo[*d*]oxazole (0.75 g, 1.47 mmol), $Pd(PPh_3)_4$ (5 mol%), K_2CO_3 (5.64 g, 5.64 mmol) in toluene/H_2O (v/v = 40 mL/10 mL) was refluxed under argon at 110 °C for overnight. After cooling to room temperature, deionized water (50 mL) was poured and organic layer was separated using a separating funnel. The water layer was washed using methylene chloride (×3) for extracted remained organic residue. After combined all of organic solvents, the organic layer was dried over anhydrous $MgSO_4$ and then filtered off. The solvent was removed under reduced pressure, and the residue was purified by silica gel column chromatography using all dichloromethane after that, ethyl acetate/*n*-hexane (v/v = 1 : 10) as the eluent and obtained white powder. Yield: 0.17 g, 29%. ^{1}H NMR (500 MHz, $CDCl_3$, ppm) δ 8.34 (d, J = 8.5 Hz, 2H), 7.85 (s, 1H), 7.82 (d, J = 9.0 Hz, 2H), 7.80–7.79 (m, 1H), 7.62–7.59 (m, 3H), 7.55–7.51 (m, 3H), 7.39–7.35 (m, 2H), 7.28 (t, J = 7.0 Hz, 4H), 7.16 (t, J = 8.5 Hz, 6H), 7.04 (t, J = 7.0 Hz, 2H). ^{13}C{^{1}H} (125 MHz, $CDCl_3$, ppm) δ 162.95, 150.84, 147.66, 147.50, 144.29, 142.24, 141.55, 140.54, 134.77, 129.38, 129.33, 128.13, 127.93, 127.68, 126.46, 126.09, 125.66, 125.65, 125.15, 124.64, 124.52, 125.86, 123.05, 120.03, 110.62. GC-MS (*m*/*z*) calcd for $C_{37}H_{26}N_2O$: 514.20, found: 514.3 $[M]^+$. Anal. calcd for $C_{37}H_{26}N_2O$: C, 86.35; H, 5.09; N, 5.44; O, 3.11. Found: C, 86.53; H, 5.12; N, 5.30; O, 3.05.

Synthesis of 4″-(benzo[*d*]thiazol-2-yl)-*N*,*N*-diphenyl-[1,1′:3′,1″-terphenyl]-4-amine (Thia)

A mixture of 3′-bromo-*N*,*N*-diphenyl-[1,1′-biphenyl]-4-amine (0.67 g, 1.68 mmol), (4-(benzo[*d*]thiazol-2-yl)phenyl)boronic acid (0.64 g, 2.51 mmol), $Pd(PPh_3)_4$ (5 mol%), K_2CO_3 (1.16 g, 8.4 mmol) in THF/H_2O (v/v = 40 mL/10 mL) was refluxed under argon at 110 °C for overnight. After cooling to room temperature, deionized water (50 mL) was poured and organic layer was separated using a separating funnel. The water layer was washed using methylene chloride (×3) for extracted remained organic residue. After combined all of organic solvents, the organic layer was dried over anhydrous $MgSO_4$ and then filtered

off. The solvent was removed under reduced pressure, and the residue was purified by silica gel column chromatography using dichloromethane/*n*-hexane (v/v = 1 : 2) as the eluent and obtained white powder. Yield: 0.67 g, 75%. ^{1}H NMR (500 MHz, $CDCl_3$, ppm) δ 8.19 (d, J = 8.5 Hz, 2H), 8.09 (d, J = 8.0 Hz, 1H), 7.92 (d, J = 8.0 Hz, 1H), 7.84 (s, 1H), 7.78 (d, J = 8.0 Hz, 2H), 7.60–7.59 (d, J = 7.5 Hz, 2H), 7.55–7.49 (m, 4H), 7.40 (t, J = 7.0 Hz, 1H), 7.28 (t, J = 8.5 Hz, 4H), 7.16 (t, J = 9.0 Hz, 6H), 7.04 (t, J = 7.0 Hz, 2H). ^{13}C{^{1}H} (125 MHz, $CDCl_3$, ppm) δ 167.70, 154.26, 147.67, 147.49, 143.79, 141.52, 140.61, 135.11, 134.81, 132.65, 129.36, 129.32, 128.04, 127.92, 127.76, 126.39, 126.35, 125.60, 125.59, 125.23, 124.52, 123.85, 123.24, 123.05, 121.64. GC-MS (m/z) calcd for $C_{37}H_{26}N_2S$: 530.18, found: 530.4 $[M]^+$. Anal. calcd for $C_{37}H_{26}N_2S$: C, 83.74; H, 4.94; N, 5.28; S, 6.04. Found: C, 83.72; H, 4.97; N, 5.26; S, 6.05.

Synthesis of 4″-(4,6-diphenyl-1,3,5-triazin-2-yl)-*N*,*N*-diphenyl-[1,1′:3′,1″-terphenyl]-4-amine (Tria)

A mixture of 3′-bromo-*N*,*N*-diphenyl-[1,1′-biphenyl]-4-amine (0.68 g, 1.70 mmol), 2,4-diphenyl-6-(4-(4,4,5,5-tetramethyl-1,3,2-dioxaborolan-2-yl)phenyl)-1,3,5-triazine (1.04 g, 2.38 mmol), $Pd(PPh_3)_4$ (5 mol%), K_2CO_3 (1.20 g, 8.50 mmol) in THF/H_2O (v/v = 40 mL/10 mL) was refluxed under argon at 110 °C for overnight. After cooling to room temperature, deionized water (50 mL) was poured and organic layer was separated using a separating funnel. The water layer was washed using methylene chloride (×3) for extracted remained organic residue. After combined all of organic solvents, the organic layer was dried over anhydrous $MgSO_4$ and then filtered off. The solvent was removed under reduced pressure, and the residue was purified by silica gel column chromatography using dichloromethane/*n*-hexane (v/v = 1 : 5) as the eluent and obtained white powder. Yield: 0.15 g, 15%. ^{1}H NMR (500 MHz, $CDCl_3$, ppm) δ 8.87 (d, J = 8.5 Hz, 2H), 8.80 (d, J = 8.5 Hz, 4H), 7.89 (s, 1H), 7.86 (d, J = 8.5 Hz, 2H), 7.66–7.53 (m, 11H), 7.29 (t, J = 8.5 Hz, 4H), 7.17 (t, J = 8.5 Hz, 6H), 7.05 (t, J = 7.5 Hz, 2H). ^{13}C{^{1}H} (125 MHz, $CDCl_3$, ppm) δ 171.70, 171.46, 147.68, 147.49, 145.28, 141.48, 140.96, 136.32, 135.31, 134.86, 132.52, 129.52, 129.33, 129.01, 128.67, 127.94, 127.45, 126.39, 125.80, 125.75, 124.53, 123.86, 123.05. GC-MS (m/z) calcd for $C_{45}H_{32}N_4$: 628.26, found: 628.5 $[M]^+$. Anal. calcd for $C_{45}H_{32}N_4$: C, 85.96; H, 5.13; N, 8.91. Found: C, 85.91; H, 5.11; N, 8.98.

Preparation of single crystal Tria

For the crystallization of dyad **Tria**, a vacuum-dried pure sample of **Tria** was taken in a vial and dissolved in CH_2Cl_2/*n*-hexane (1 : 1) mixed solvent; by the slow evaporation at room temperature for about 4 weeks, a white **Tria** single crystal was obtained. Then the crystals were picked up from the vial and a single-crystal XRD study was performed.

X-ray crystal structure analysis

The data were collected at 223(2) K using a Bruker D8 Venture equipped with IμS micro-focus sealed tube Mo Kα (λ = 0.71073 Å) and a PHOTON II 14 detector in Western Seoul Center of Korea Basic Science Institute. Preliminary unit cell constants were determined using a set of 45 narrow-frame (0.3° in ω) scans. The double pass method of scanning was used to exclude noise. Collected frames were integrated using an orientation matrix determined from narrow-frame scans. The SMART software package was used for data collection, and SAINT was used for frame integration.[71] Final cell constants were determined by global refinement of *xyz* centroids of reflections harvested from the entire data set. Structure solution and refinement were carried out using the SHELXTL-PLUS software package.[72] The crystallographic information has been deposited with the Cambridge Crystallographic Data Centre and assigned the CCDC code 2091706 for **Tria**.

Photophysical measurements

The UV/vis absorption spectra were recorded using a Sinco Mega-2100 spectrophotometer in dual beam mode, and the fluorescence emission measurements were carried out using Shimadzu fluorometer (RF-6000) with a wavelength resolution of ~1 nm. Fluorescence lifetimes were measured by PicoQuant FluoTime 200 that takes advantage of the time-correlated single photon counting method. A pulsed diode laser operated at 20 MHz repetition rate was used as the excitation source. The FWHM of a laser pulse was typically 45 ps, and the instrument response function was ~190 ps when the Hamamatsu photomultiplier tube (H5783-01) was used. The emission quantum yields (Φ_{PL}) were calculated using William's comparative method for samples of five different concentrations of (1–5) μM, using 9,10-diphenylanthracene (Φ_{PL} = 0.95, ethanol) as a reference standard.[73]

Cyclic voltammetry (CV)

A CH Instruments 701D potentiostat was used for electrochemical measurements, and cyclic voltammetry (CV) was performed in an electrolytic solution prepared using 1 mM of electroactive compounds and 0.1 M tetrabutylammonium perchlorate (Bu_4NClO_4) in deoxygenated dichloromethane and THF. A three-electrode configuration, glassy carbon, platinum wire, and SCE were used as working, counter, and reference electrodes, respectively.

Density functional theory calculations

Density functional theory (DFT) calculations were performed by using Gaussian' 16 software package. Full geometry optimizations in their ground state were performed using the B3LYP functional and the 6-31G(d,p) basis set for all atoms. The excitation energies and oscillator strengths for the lowest 100 singlet–singlet transitions at the optimized geometry in the ground state were obtained in time-dependent DFT (TD-DFT) calculations using the same basis set and functional as for the ground state. All isodensity plots of the frontier orbitals were visualized by Chem3D Ultra and GaussView software. More detail DFT/TD-DFT calculation results for all dyads are described in ESI.†

Author contributions

M.-J. Kim, M. Ahn, M. Chae, S. Kim, and D. Kim prepared/performed the experiment including DFT calculations and

prepared figures. M.-J. Kim and K.-R. Wee planned the experiment and wrote the paper. All authors contributed to the paper with discussions and edits.

Conflicts of interest

There are no conflicts to declare.

Acknowledgements

This research was supported by the Basic Science Research Program through the National Research Foundation of Korea (NRF-2020R1C1C1009007) and Korea Basic Science Institute (National Research Facilities and Equipment Center) grant, funded by the Ministry of Education (2020R1A6C103A028).

Notes and references

1 M. T. Colvin, A. B. Ricks and M. R. Wasielewski, *J. Phys. Chem. A*, 2012, **116**, 2184–2191.
2 W. Yang and Y. Li, *Dyes Pigm.*, 2016, **125**, 100–105.
3 M. Ito, E. Ito, M. Hirai and S. Yamaguchi, *J. Org. Chem.*, 2018, **83**, 8449–8456.
4 P. Das, A. Kumar, A. Chowdhury and P. S. Mukherjee, *ACS Omega*, 2018, **3**, 13757–13771.
5 R. Rani, G. Kumar, K. Paul and V. Luxami, *New J. Chem.*, 2018, **42**, 12729–12736.
6 J. Van Damme, O. van den Berg, J. Brancart, G. Van Assche and F. Du Prez, *Tetrahedron*, 2019, **75**, 912–920.
7 C. Wu, Z. Wu, B. Wang, X. Li, N. Zhao, J. Hu, D. Ma and Q. Wang, *ACS Appl. Mater. Interfaces*, 2017, **9**, 32946–32956.
8 H. Sun, X. Song, J. Xie, P. Sun, P. Gu, C. Liu, F. Chen, Q. Zhang, Z.-K. Chen and W. Huang, *ACS Appl. Mater. Interfaces*, 2017, **9**, 29924–29931.
9 J. Zhang, J. Jin, H. Xu, Q. Zhang and W. Huang, *J. Mater. Chem. C*, 2018, **6**, 3485–3498.
10 E. V. Verbitskiy, Y. A. Kvashnin, P. I. Bogdanov, M. V. Medvedeva, T. S. Svalova, A. N. Kozitsina, L. G. Samsonova, K. M. Degtyarenko, D. V. Grigoryev and A. E. Kurtcevich, *Dyes Pigm.*, 2021, **187**, 109124.
11 R. Furue, K. Matsuo, Y. Ashikari, H. Ooka, N. Amanokura and T. Yasuda, *Adv. Opt. Mater.*, 2018, **6**, 1701147.
12 X. Liang, Z. Wang, L. Wang, M. Hanif, D. Hu, S. Su, Z. Xie, Y. Gao, B. Yang and Y. Ma, *Chin. J. Chem.*, 2017, **35**, 1559–1568.
13 S. Thurakkal, K. S. Sanju, A. Soman, K. N. Unni, J. Joseph and D. Ramaiah, *New J. Chem.*, 2018, **42**, 5456–5464.
14 C. Poriel and J. Rault-Berthelot, *Adv. Funct. Mater.*, 2021, 2010547.
15 C. c. Peng, S. y. Yang, H. c. Li, G. h. Xie, L. s. Cui, S. N. Zou, C. Poriel, Z. Q. Jiang and L. s. Liao, *Adv. Mater.*, 2020, **32**, 2003885.
16 F. Lucas, O. A. Ibraikulov, C. Quinton, L. Sicard, T. Heiser, D. Tondelier, B. Geffroy, N. Leclerc, J. Rault-Berthelot and C. Poriel, *Adv. Opt. Mater.*, 2020, **8**, 1901225.
17 J.-H. Lee, C.-H. Chen, P.-H. Lee, H.-Y. Lin, M.-k. Leung, T.-L. Chiu and C.-F. Lin, *J. Mater. Chem. C*, 2019, **7**, 5874–5888.
18 A. Mishra, M. K. Fischer and P. Bäuerle, *Angew. Chem., Int. Ed.*, 2009, **48**, 2474–2499.
19 W. J. Shi, T. Kinoshita and D. K. Ng, *Asian J. Org. Chem.*, 2017, **6**, 758–767.
20 Y. Ooyama, Y. Hagiwara, Y. Oda, T. Mizumo, Y. Harima and J. Ohshita, *New J. Chem.*, 2013, **37**, 2336–2340.
21 A. Pallikkara and K. Ramakrishnan, *Int. J. Energy Res.*, 2021, **45**, 1425–1448.
22 A. Leliège, J. Grolleau, M. Allain, P. Blanchard, D. Demeter, T. Rousseau and J. Roncali, *Chem.–Eur. J.*, 2013, **19**, 9948–9960.
23 Y. Cui, P. Li, C. Song and H. Zhang, *J. Phys. Chem. C*, 2016, **120**, 28939–28950.
24 Y. N. Luponosov, A. N. Solodukhin, A. L. Mannanov, V. A. Trukhanov, S. M. Peregudova, S. A. Pisarev, A. V. Bakirov, M. A. Shcherbina, S. N. Chvalun and D. Y. Paraschuk, *Org. Electron.*, 2017, **51**, 180–189.
25 E. Aslan, M. Karaman, G. Yanalak, H. Bilgili, M. Can, F. Ozel and I. H. Patir, *J. Photochem. Photobiol., A*, 2020, **390**, 112301.
26 B. D. Sherman, M. V. Sheridan, K.-R. Wee, S. L. Marquard, D. Wang, L. Alibabaei, D. L. Ashford and T. J. Meyer, *J. Am. Chem. Soc.*, 2016, **138**, 16745–16753.
27 K.-R. Wee, B. D. Sherman, M. K. Brennaman, M. V. Sheridan, A. Nayak, L. Alibabaei and T. J. Meyer, *J. Mater. Chem. A*, 2016, **4**, 2969–2975.
28 D. L. Ashford, M. K. Gish, A. K. Vannucci, M. K. Brennaman, J. L. Templeton, J. M. Papanikolas and T. J. Meyer, *Chem. Rev.*, 2015, **115**, 13006–13049.
29 Q. Li, Z. Wang, W. Song, H. Ma, J. Dong, Y.-Y. Quan, X. Ye and Z.-S. Huang, *Dyes Pigm.*, 2019, **161**, 389–395.
30 S.-Y. Kim, M.-J. Kim, M. Ahn, K.-M. Lee and K.-R. Wee, *Dyes Pigm.*, 2021, **191**, 109362.
31 J.-P. Malval, M. Cranney, S. Achelle, H. Akdas-Kiliç, J.-L. Fillaut, N. Cabon, F. Robin-le Guen, O. Soppera and Y. Molard, *Chem. Commun.*, 2019, **55**, 14331–14334.
32 S. Zhang, H. Zhu, J. Huang, L. Kong, Y. Tian and J. Yang, *ChemistrySelect*, 2019, **4**, 7380–7387.
33 Y. Gong, Y. Tan, J. Liu, P. Lu, C. Feng, W. Z. Yuan, Y. Lu, J. Z. Sun, G. He and Y. Zhang, *Chem. Commun.*, 2013, **49**, 4009–4011.
34 M.-J. Kim, M. Ahn and K.-R. Wee, *Mater. Adv.*, 2021, **2**, 5371–5380.
35 P. Vineetha, A. Aswathy, E. Shiju, K. Chandrasekharan and N. Manoj, *New J. Chem.*, 2020, **44**, 6142–6150.
36 C.-Z. Zhang, C. Lu, J. Zhu, G.-Y. Lu, X. Wang, Z.-W. Shi, F. Liu and Y. Cui, *Chem. Mater.*, 2006, **18**, 6091–6093.
37 K. Kannan, D. Radhika, A. Nesaraj, K. K. Sadasivuni, K. R. Reddy, D. Kasai and A. V. Raghu, *Mater. Sci. Energy Technol.*, 2020, **3**, 853–861.
38 R. Prabhu, T. Jeevananda, K. R. Reddy and A. V. Raghu, *Mater. Sci. Energy Technol.*, 2021, **4**, 107–112.
39 K. R. Reddy, B. Hemavathi, G. R. Balakrishna, A. Raghu, S. Naveen and M. Shankar, in *Polymer Composites with Functionalized Nanoparticles*, Elsevier, 2019, pp. 357–379.

40 Y.-J. Cho, A.-R. Lee, S.-Y. Kim, M. Cho, W.-S. Han, H.-J. Son, D. W. Cho and S. O. Kang, *Phys. Chem. Chem. Phys.*, 2016, **18**, 22921–22928.
41 D. Thirion, M. Romain, J. Rault-Berthelot and C. Poriel, *Mater. Adv.*, 2021, **2**, 1271–1283.
42 S. Delmond, J.-F. Létard, R. Lapouyade and W. Rettig, *J. Photochem. Photobiol., A*, 1997, **105**, 135–148.
43 X. Niu, P. Gautam, Z. Kuang, P. Y. Craig, Y. Guo, H. Song, Q. Guo, J. M. Chan and A. Xia, *Phys. Chem. Chem. Phys.*, 2019, **21**, 17323–17331.
44 M. Ahn, M.-J. Kim, D. W. Cho and K.-R. Wee, *J. Org. Chem.*, 2020, **86**, 403–413.
45 M. Harrison and R. Friend, in *Electronic Materials: The Oligomer Approach*, Wiley-VCH, Weinheim, 1998, pp. 515–558.
46 M.-J. Kim, M. Ahn, J. H. Shim and K.-R. Wee, *Phys. Chem. Chem. Phys.*, 2020, **22**, 3370–3378.
47 H. Liu, Q. Bai, L. Yao, H. Zhang, H. Xu, S. Zhang, W. Li, Y. Gao, J. Li and P. Lu, *Chem. Sci.*, 2015, **6**, 3797–3804.
48 M. Romain, S. Thiery, A. Shirinskaya, C. Declairieux, D. Tondelier, B. Geffroy, O. Jeannin, J. Rault-Berthelot, R. Métivier and C. Poriel, *Angew. Chem., Int. Ed.*, 2015, **54**, 1176–1180.
49 C. Lu, C. Long, Y. Li, Z. Li and H. Zhu, *J. Membr. Sci.*, 2020, **598**, 117797.
50 Q. Wang, F. Lucas, C. Quinton, Y.-K. Qu, J. Rault-Berthelot, O. Jeannin, S.-Y. Yang, F.-C. Kong, S. Kumar and L.-S. Liao, *Chem. Sci.*, 2020, **11**, 4887–4894.
51 S. F. Swallen, Z.-Y. Shi, W. Tan, Z. Xu, J. S. Moore and R. Kopelman, *J. Lumin.*, 1998, **76**, 193–196.
52 C. Gao, S. K. Prasad, B. Zhang, M. Dvořák, M. J. Tayebjee, D. R. McCamey, T. W. Schmidt, T. A. Smith and W. W. Wong, *J. Phys. Chem. C*, 2019, **123**, 20181–20187.
53 P. Guiglion and M. A. Zwijnenburg, *Phys. Chem. Chem. Phys.*, 2015, **17**, 17854–17863.
54 L. Sicard, C. Quinton, J. D. Peltier, D. Tondelier, B. Geffroy, U. Biapo, R. Métivier, O. Jeannin, J. Rault-Berthelot and C. Poriel, *Chem.–Eur. J.*, 2017, **23**, 7719–7727.
55 L.-S. Cui, S.-C. Dong, Y. Liu, M.-F. Xu, Q. Li, Z.-Q. Jiang and L.-S. Liao, *Org. Electron.*, 2013, **14**, 1924–1930.
56 C. Poriel and J. Rault-Berthelot, *Acc. Chem. Res.*, 2018, **51**, 1818–1830.
57 N. Metri, X. Sallenave, C. d. Plesse, L. Beouch, P.-H. Aubert, F. Goubard, C. Chevrot and G. Sini, *J. Phys. Chem. C*, 2012, **116**, 3765–3772.
58 J. Zhang, D. Deng, C. He, Y. He, M. Zhang, Z.-G. Zhang, Z. Zhang and Y. Li, *Chem. Mater.*, 2011, **23**, 817–822.
59 J. Lee, K. Shizu, H. Tanaka, H. Nakanotani, T. Yasuda, H. Kaji and C. Adachi, *J. Mater. Chem. C*, 2015, **3**, 2175–2181.
60 S.-H. Chen, K. Jiang, Y. Xiao, X.-Y. Cao, M. Arulkumar and Z.-Y. Wang, *Dyes Pigm.*, 2020, **175**, 108157.
61 I. M. Paczkowski, F. L. Coelho and L. F. Campo, *J. Mol. Liq.*, 2020, **319**, 114277.
62 A. B. Morgan, J. L. Jurs and J. M. Tour, *J. Appl. Polym. Sci.*, 2000, **76**, 1257–1268.
63 A. Raghu, G. Gadaginamath, N. Mathew, S. Halligudi and T. Aminabhavi, *J. Appl. Polym. Sci.*, 2007, **106**, 299–308.
64 A. Raghu, G. Gadaginamath, M. Priya, P. Seema, H. M. Jeong and T. Aminabhavi, *J. Appl. Polym. Sci.*, 2008, **110**, 2315–2320.
65 J. E. Campbell, J. Yang and G. M. Day, *J. Mater. Chem. C*, 2017, **5**, 7574–7584.
66 M. Kasha, *Radiat. Res.*, 1963, **20**, 55–70.
67 N. Mataga, Y. Kaifu and M. Koizumi, *Bull. Chem. Soc. Jpn.*, 1956, **29**, 465–470.
68 B. Pramodh, P. Naresh, S. Naveen, N. Lokanath, S. Ganguly, J. Panda, S. Murugesan, A. Raghu and I. Warad, *Chem. Data Collect.*, 2021, **31**, 100587.
69 S. B. Prasad, S. Naveen, C. A. Kumar, N. Lokanath, A. Raghu, I. Daraghmeh, K. R. Reddy and I. Warad, *J. Mol. Struct.*, 2018, **1167**, 215–226.
70 S. B. Prasad, C. Anandakumar, A. Raghu, K. R. Reddy, M. D. Urs and S. Naveen, *Chem. Data Collect.*, 2018, **15**, 1–9.
71 G. Sheldrick, *SMART and SAINT*, Bruker Analytical X-ray Division, Madison, WI, 2001.
72 G. Sheldrick, *SHELXTL-PLUS Software Package*, Bruker Analytical X-Ray Division, Madison, WI, 2002.
73 J. V. Morris, M. A. Mahaney and J. R. Huber, *J. Phys. Chem.*, 1976, **80**, 969–974.